scientific reports

Check for updates

OPEN

Highly defective graphene quantum dots-doped 1T/2H-MoS_2 as an efficient composite catalyst for the hydrogen evolution reaction

Sheng-Fu Chen[1], Tai-Sing Wu[2]✉ & Yun-Liang Soo[1,2]✉

We present a new composite catalyst system of highly defective graphene quantum dots (HDGQDs)-doped 1T/2H-MoS_2 for efficient hydrogen evolution reactions (HER). The high electrocatalytic activity, represented by an overpotential of 136.9 mV and a Tafel slope of 57.1 mV/decade, is due to improved conductivity, a larger number of active sites in 1T-MoS_2 compared to that in 2H-MoS_2, and additional defects introduced by HDGQDs. High-resolution transmission electron microscopy (HRTEM), Raman spectroscopy, x-ray diffraction (XRD) and x-ray photoelectron spectroscopy (XPS) were used to characterize both the 1T/2H-MoS_2 and GQDs components while Fourier-transform infrared spectroscopy (FTIR) was employed to identify the functional groups on the edge and defect sites in the HDGQDs. The morphology of the composite catalyst was also examined by field emission scanning electron microscopy (FESEM). All experimental data demonstrated that each component contributes unique advantages that synergistically lead to the significantly improved electrocatalytic activity for HER in the composite catalyst system.

Electrocatalytic hydrolysis is considered as one of the most environmentally friendly methods for hydrogen production due to its non-polluting and recyclable nature. In search of high-performance and low-cost catalysts for electrochemical hydrogen evolution reactions (HER), transition metal dichalcogenides have been noted to be favorable candidates owing to their unique two-dimensional properties that can improve catalytic capability. In the present work, we are especially interested in the MoS_2 system, which has been demonstrated to have excellent HER catalytic activity and low-onset overpotential.[1,2] The electrical conductivity and the number of active sites from sulfur vacancies, which are on the edges in 2H- and 1T-MoS_2 [3] and on the basal plane in 1T-MoS_2[4], are the two main factors that determine the catalytic efficiency of the material. The most stable form, 2H-MoS_2, is a semiconductor with low carrier transport efficiency and poor electrical conductivity that restrict its catalytic performance.[5] To improve electrical conductivity, many studies have focused on using the metallic 1T phase to replace the semiconducting 2H phase of MoS_2.[6–9] However, the 1T phase of MoS_2 is unstable and can easily transition to the 2H phase. Alternatively, the catalytic performance of MoS_2 may be improved by decorating its active sites. In particular, graphene quantum dots (GQDs) are used to introduce numerous defects on the active sites of MoS_2, enhancing the electrical conductivity and catalytic activity.[10–12] However, the hydrothermal method, usually used for incorporating GQDs into MoS_2, can easily induce 1T-to-2H phase transition in the MoS_2 host due to the elevated temperature above 190°C used in the process.[10] Therefore, recent studies on GQD-doped MoS_2 have been mainly based on the 2H phase.[10,13].

In this paper, we present an easy method to prepare a new composite catalyst system: a combination of a carbon paper as the substrate, highly defective GQDs (HDGQDs) as an enhancer, and 1T/2H-MoS_2 as the main catalytic agent. The 1T/2H-MoS_2 was prepared by a Li-ion intercalation process, while the HDGQDs were fabricated from citric acid using the pyrolysis carbonization method. The HDGQDs and 1T/2H-MoS_2 solutions were then dropped and air-dried on the carbon paper to form the composite catalyst system. We note that no additional heating was required to combine the HDGQDs with MoS_2 and the 1T phase of MoS_2 was successfully preserved. The three goals of improving electrical conductivity, increasing the number of active sites, and enhancing the catalytic performance of the active sites are therefore simultaneously accomplished. Our 1T/2H-MoS_2/HDGQDs catalyst exhibits excellent HER electrocatalytic performance. This work provides a unique new strategy for the preparation of high-performance water electrolysis catalysts.

[1]Department of Physics, National Tsing Hua University, Hsinchu, Taiwan. [2]National Synchrotron Radiation Research Center, Hsinchu, Taiwan. ✉email: wu.ts@nsrrc.org.tw; soo@phys.nthu.edu.tw

Methods

The 1T/2H-MoS_2/HDGQDs composite catalyst system was fabricated by sequentially dropping the HDGQDs (0.2 ml, 6 mg/ml) or GQDs (0.0545 ml, 22 mg/ml)[14] and 1T/2H-MoS_2 solutions (0.2 ml) onto the carbon paper substrate (CeTech, GPP035), covering a circular area of radius 0.3 cm, and then letting them air dry. The dosages for 1T/2H-MoS_2 and HDGQDs were tested to achieve optimal loading, with further details provided in the supplementary information. As shown in Supplementary Figure S1, S2 and Table S1, we determined that 0.2 ml of MoS_2 is the optimal loading on the Carbon paper as the primary catalytic agent. When the MoS_2 loading exceeds 0.2 ml, the efficiency decreases due to increased resistance, which hinders the hydrogen evolution reaction. As depicted in Supplementary Figure S3, we found that 0.2 ml of HDGQDs is the optimal loading for enhancing the MoS_2 catalyst. Further addition of HDGQDs does not increase efficiency, as the active sites of MoS_2 are already saturated.

To prepare the HDGQDs solution, citric acid powders (2 g) in a glass flask were oil-bath heated to 200℃ for 30 min. The orange liquid of pyrolyzed citric acid was mixed with deionized water (20 ml) to form a HDGQDs solution, which was then purified by filtering using a 0.22 μm microporous membrane and dialyzed using a cellulose ester membrane bag (flat width 54 mm, diameter 34 mm, MWCO 3.5 KD) for two days, with several water changes during the dialysis process. For comparison, we also fabricated standard GQDs by increasing the heating time from 30 to 90 min in the above process.

The 1T/2H-MoS_2 solution was prepared by using an improved lithium ion intercalation-based exfoliation process. Molybdenum (IV) sulfide 99% powders of 90 nm-diameter (0.1 g) and n-Butyl lithium (5 ml) were mixed in an autoclave reactor and heated to 110℃ in an oven for 12 h. In contrast to the previous method, where 0.5 g bulk MoS_2 powder was soaked in 4 ml of 1.6 M n-butyllithium/hexane for 48 hours[15], this approach can significantly enhance the efficiency of lithium ion insertion. After cooling down to room temperature, the mixture was diluted in n-hexane and centrifuged to remove excessive n-Butyl lithium not intercalated with MoS_2, leaving the Li_xMoS_2 as precipitates. Hydrochloric acid solution (150 ml, pH = 3) was then added to exfoliate MoS_2 few layer sheets from the Li_xMoS_2 precipitates. Finally, the MoS_2 solution was purified by centrifugation, filtration (pore size 0.22 μm, CA membrane filter) and dialysis (Peristaltic pump rapid dialysis device, MWCO 12–14 kD hollow fiber) to obtain a neutral 1T/2H-MoS_2 solution. Compared to the previous method, where hydrochloric acid solution was dropwise added to an alkaline MoS_2 colloidal solution containing trace amounts of lithium hydroxide until the pH reached around 7[15], this milder dialysis approach avoids residual chloride ions and exothermic acid–base reactions. This prevents phase change and oxidation of MoS_2. On the other hand, the milder dialysis approach can effectively remove LiOH and concentrate the sample according to experimental requirements. For the Raman and XPS measurements, the solution was dropped on a carbon paper substrate and air dried to form the 1T/2H-MoS_2 sample. A more thermally stable 2H-MoS_2 sample was also prepared by heating the 1T/2H-MoS_2 sample at 300℃ for 1 h in vacuum[16].

To characterize the GQDs and 1T/2H-MoS_2 components of the composite catalysts, a high-resolution transmission electron microscope (HR-TEM) (JEOL JEM-2010) with acceleration voltage 200 kV was used to probe the microstructures. Raman spectra were obtained using a Raman spectrometer with a CCD camera (HORIBA, iHR-550) and a 514 nm excitation laser. The Raman band for Si at ~ 520.7 cm^{-1} was used as a reference to calibrate the spectrometer. The x-ray diffraction (XRD) patterns in the 2θ range of 5–40° were recorded on an in-house x-ray diffractometer (Bruker, D8 discover plus) using the Cu-Kα radiation ($\lambda = 0.15418$ nm). Fourier-transform infrared spectroscopy (FTIR) was also obtained, by using an FT-IR spectrophotometer (Bruker, Vertex80v), to identify the functional groups on the edge and defect sites in the HDGQDs sample. The chemical environments surrounding C and O in GQDs and Mo and S in MoS_2 were investigated by x-ray photoelectron spectroscopy (ULVAC-PHI, PHI Quantera II, with binding energies corrected using the C 1 s peak of 284.5 eV). Finally, the morphologies of the composite catalyst systems were examined by field emission scanning electron microscopy (FE-SEM) (JEOL 7900F).

Electrochemical analyses including linear sweep voltammetry (LSV), Tafel plots, electrochemical impedance spectroscopy (EIS), and stability test were carried out to evaluate the electrocatalytic activity for the new composite catalyst system of 1T/2H-MoS_2/HDGQDs on carbon paper substrate. An electrolytic cell with the electrocatalyst, an Ag/AgCl electrode, and a glassy carbon electrode as the working, reference, and counter electrodes, respectively, submerged in a 0.5 M H_2SO_4 electrolyte solution was connected to a CHI electrochemical workstation (CHI Instruments 760D) for all the electrochemical measurements. The LSV curves were scanned with a scan rate of 5 mV/s. The LSV curve of a blank carbon paper substrate was also measured to perform background subtraction and baseline correction for all samples[17].A 1.5 Ω small series resistance is used to treat LSV curves for iR correction[18]. The electrochemical potentials in these measurements were converted to the reversible hydrogen electrode (RHE) scale[19]. Using the Tafel equation, Tafel plots were also obtained from the LSV data to calculate the Tafel slopes[20]. The EIS data were measured at an overpotential of − 0.3 V vs. RHE in the frequency range of 0.001 ~ 100 kHz with an amplitude of 5 mV[10,12]. Chronopotentiometry experiments were carried out in a 0.5 M H_2SO_4 solution with a constant current density of 10 mA/cm^2.

Results and discussion

As demonstrated in Fig. 1a, the TEM micrograph shows that the particle size of the HDGQDs is around 3-5 nm. The graphite (1120) planes with a d-spacing of 0.22nm[21] can also be clearly seen in the high-resolution TEM (HRTEM) micrograph (Fig. 1b). However, no clear pattern was observed in the fast Fourier transform of the micrograph, probably due to the material's highly defective structure. In contrast, as shown in Fig. 1c, the TEM micrograph of the standard GQDs sample exhibits an appreciably larger particle size of 20 nm and its fast Fourier transform shows clear pattern of six-fold symmetry[22] (Fig. 1d), indicating that the increased heating time of 90 min can effectively eliminate defects and enlarge graphene particles at the same time.

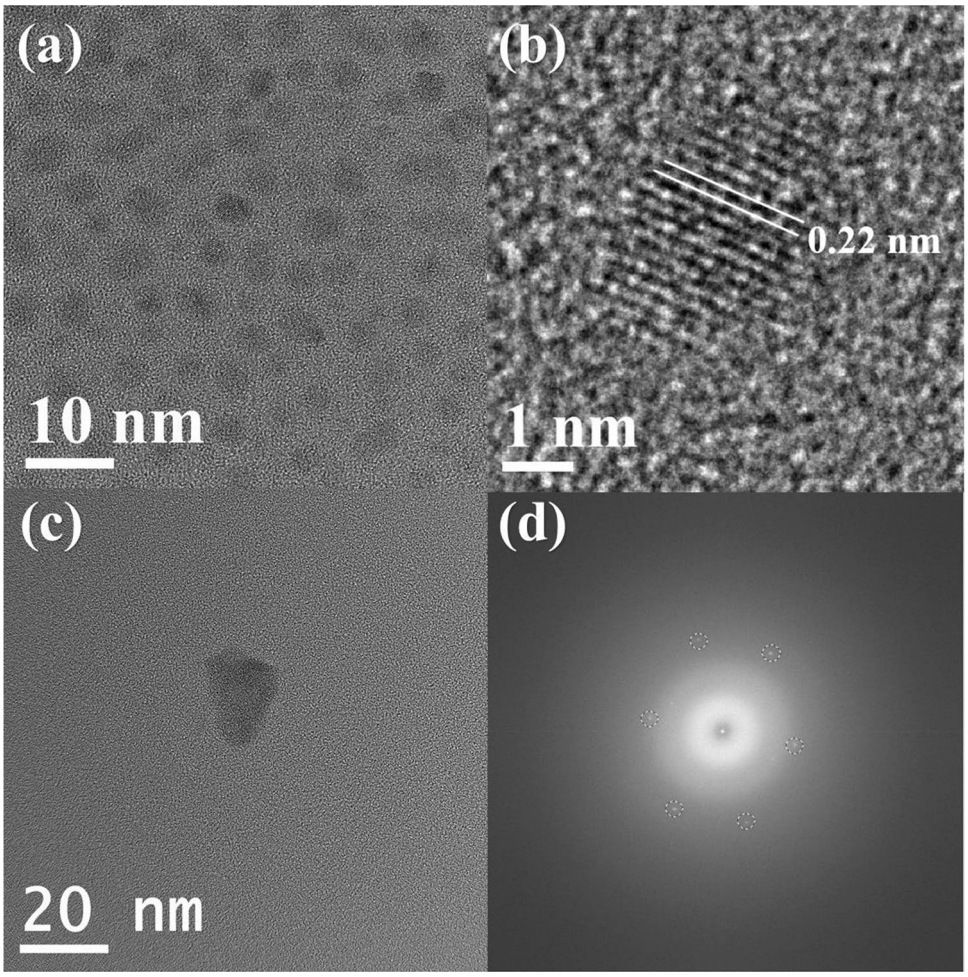

Figure 1. (**a**) TEM micrograph of HDGQDs. (**b**) HRTEM micrograph of HDGQDs. (**c**) TEM micrograph of standard GQDs. (**d**) FFT pattern of standard GQDs.

The Raman spectroscopy measurements can be used to compare the number of defects in the HDGQDs with that in the standard GQDs. As demonstrated in Fig. 2a, two peaks are present in the spectra of both the HDGQDs and standard GQD samples. The peaks at 1355 cm^{-1} and 1595 cm^{-1} are attributed to the D band and G band which represent the defect-related out-of-plane vibration and the in-plane sp^2 mode of graphene, respectively. Therefore, the ratio of peak intensities of the D and G bands can be used to evaluate the defective structure of the sample[23]. The D/G ratio of 2.56 for the HDGQDs sample is appreciably higher than that of 1.70 for the standard GQDs sample. The Raman spectroscopy results demonstrate that the number of defects in GQDs samples fabricated from pyrolyzing citric acid can be controlled by adjusting the heating time.

As shown in Fig. 2b, peaks at 3585 cm^{-1}, 1724 cm^{-1}, 1083 cm^{-1}, and 1402 cm^{-1}, representing the stretching vibrations of O-H[14,21,24–26], C = O[14,26], C-O[21,24], and in-plane bending vibration of O-H[14,21,24,25] in the carboxyl groups, respectively, appear in the FTIR spectrum. A peak at 1637 cm^{-1} ascribed to skeletal ring vibrations of aromatic C = C[21,25] in the graphitic domain and a peak at 1230 cm^{-1} attributed to stretching vibrations of C-O[14,24,25] in the -COC bond, are also present.

X-ray photoelectron spectroscopy (XPS) was used to identify the chemical environments of carbon and oxygen atoms in the HDGQDs sample. As shown in Fig. 2c, three peaks centered at 288.5 eV, 286.3 eV and 284.6 eV assigned to O = C-O, C-O/C–O–C, and sp^2 C = C bonding, respectively, were observed in the C1s spectrum[11,13,21,27–29]. In the O1s spectrum shown in Fig. 2d, the peaks at 535.6 eV, 532.3 and 530.9 eV are attributed to the C–O–H, C–O, and C = O bonding, respectively[27]. The chemical bonding of C and O revealed by XPS measurements is consistent with the presence of the functional groups observed from FTIR data in the HDGQDs samples (Fig. 2b).

As shown in Fig. 3a, the particle size of 1T/2H-MoS_2 revealed by the TEM micrograph is around 20–40 nm, substantially larger than the HDGQDs size of 3–5 nm. The Raman data plotted in Fig. 3b shows that both the 1T/2H-MoS_2 and 2H-MoS_2 spectra have two major peaks: a peak at 379.4 or 381.5 cm^{-1} (E^1_{2g}), representing the vibration of two sulfur atoms with respect to molybdenum, and a peak at 401.0 or 4.03,8 cm^{-1} (A_{1g}), representing the relative vibration of S atoms in the out of plane direction[8]. However, the 1T/2H-MoS_2 spectrum exhibits four additional peaks at 146.8 cm^{-1}(J_1), 237.6 cm^{-1}(J_2), 283.7 cm^{-1}(E_{1g}), and 334.7 cm^{-1}(J_3)[6]. The E_{1g} mode is

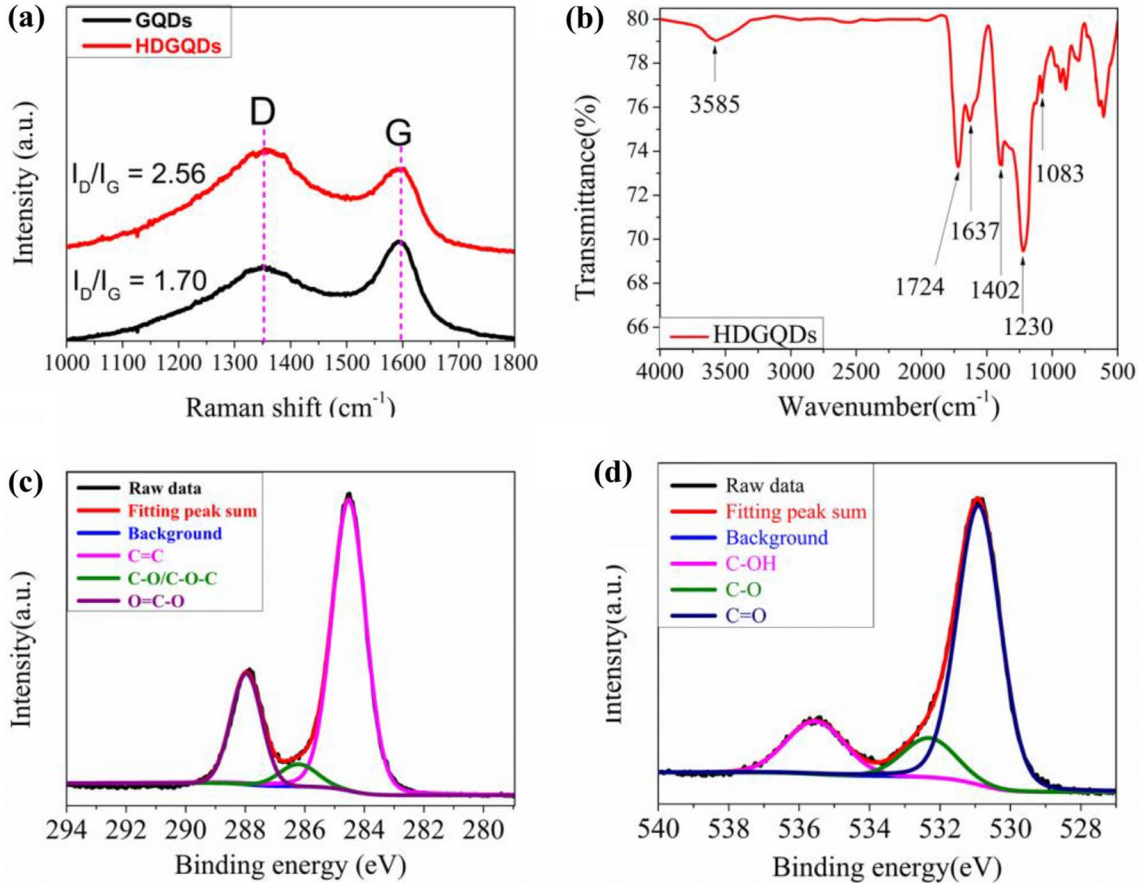

Figure 2. (**a**) Raman spectra of HDGQDs and GQDs. (**b**) FTIR spectrum of HDGQDs. (**c**) High-resolution C1s XPS spectra of HDGQDs. (**d**) High-resolution O1s XPS spectra of HDGQDs.

attributed to the octahedral coordination of Mo in 1T-MoS_2[30] while the J_1, J_2, and J_3 modes are due to the superlattice structure of 1T-MoS_2[31]. Therefore, the Raman results indicate that our 1T/2H-MoS_2 sample indeed contains both the 1T-MoS_2 and 2H-MoS_2 phases.

Figure 3c shows the XRD patterns of the 1T/2H-MoS_2 and 2H-MoS_2 samples. A diffraction peak centered at around 15.0° corresponding to the (002) planes of the 2H-MoS_2 structure appeared in the data of the 2H-MoS_2 samples. On the other hand, three peaks at around 7.8°, 11.6° and 15.1° representing the 1T (001), 1T (002) and 2H (002) planes, respectively, were observed in the data of the 1T/2H-MoS_2 sample[32–34]. According to the Scherrer equation, $D = \kappa\lambda/\beta\cos(\theta)$, where $\kappa = 0.9$ and $\lambda = 0.154056$ (nm), the grain size for the 2H-MoS_2 sample with 2H (002) peak position $2\theta = 15.0°$ and peak width $\beta = 1.44°$ was estimated to be 5.6 nm. For the 1T/2H-MoS_2 sample, the 1T-MoS_2 grain size calculated from the 1T(001) peak at $2\theta = 7.8°$ with $\beta = 1.87°$ is 4.3 nm while the 2H-MoS_2 grain size calculated from the 2H (002) peak at $2\theta = 15.1°$ with $\beta = 1.84°$ is 4.4 nm. We note that the grain size obtained from the XRD patterns for the MoS_2 samples are a lot smaller than the particle size observed in the TEM micrograph. This indicates that the smaller MoS_2 grains that give rise to the broader XRD peaks have combined to form larger aggregates seen in the TEM micrograph. From the above XRD results, we can confirm that our 2H-MoS_2 sample has pure 2H phase and our 1T/2H-MoS_2 sample has both 1T phase and 2H phase.

The XPS analysis was also used to estimate the phase compositions in the 1T/2H-MoS_2 and 2H-MoS_2 samples (Fig. 3d–g). Deconvolution of the XPS spectra was performed using the XPSPEAK41 package[35]. We observed four peaks assigned to Mo^{6+} $3d_{3/2}$, Mo^{6+} $3d_{5/2}$& Mo^{4+} $3d_{3/2}$, Mo^{4+} $3d_{5/2}$, and S 2s[7,8,28,29,36] in the XPS spectra of Mo 3d for both samples. In the spectrum for the 1T/2H-MoS_2 sample (Fig. 3d), the Mo^{4+} $3d_{5/2}$, and Mo^{4+} $3d_{3/2}$ peaks for the 1T-MoS_2 phase are located at 228.31 and 231.51 eV, while those for the 2H-MoS_2 phase are at 229.31 and 232.51 eV, respectively. The S 2s peak at 225.61 eV for MoS_2, as well as the $Mo^{6+}3d_{5/2}$ peak at 231.64 eV and the Mo^{6+} $3d_{3/2}$ peak at 234.84 eV, both representing an MoO_3 impurity in the MoS_2 sample, are also present. From the fitted peak area ratios, the 1T/2H-MoS_2 sample was found to be composed of 60.79% 1T-MoS_2, 30.45% 2H-MoS_2, and 8.76% MoO_3. In the spectrum for the 2H-MoS_2 sample (Fig. 3f), we can see that the 1T-MoS_2 peaks have disappeared due to the heating process. Apart from the S 2s peak at 226.41 eV, the 2H-MoS_2 peaks at 229.27 and 233.41 eV, and the impurity MoO_3 peaks at 232.27 and 235.41 eV are found in the spectrum. The ratios of 2H-MoS_2 and MoO_3 in the sample were estimated to be 90.25% and 9.75%, respectively. We also observed two peaks assigned to S $2p_{1/2}$ and S $2p_{3/2}$[7,8,28,29,36] in the XPS spectra of S 2p for both samples. In the spectrum for the 1T/2H-MoS_2 sample (Fig. 3e), the S $2p_{1/2}$, and S $2p_{3/2}$ peaks for the 1T-MoS_2 phase are located at 162.19 and 161.06 eV, while those for the 2H-MoS_2 phase are at 163.19 and 162.06 eV, respectively. From the fitted peak

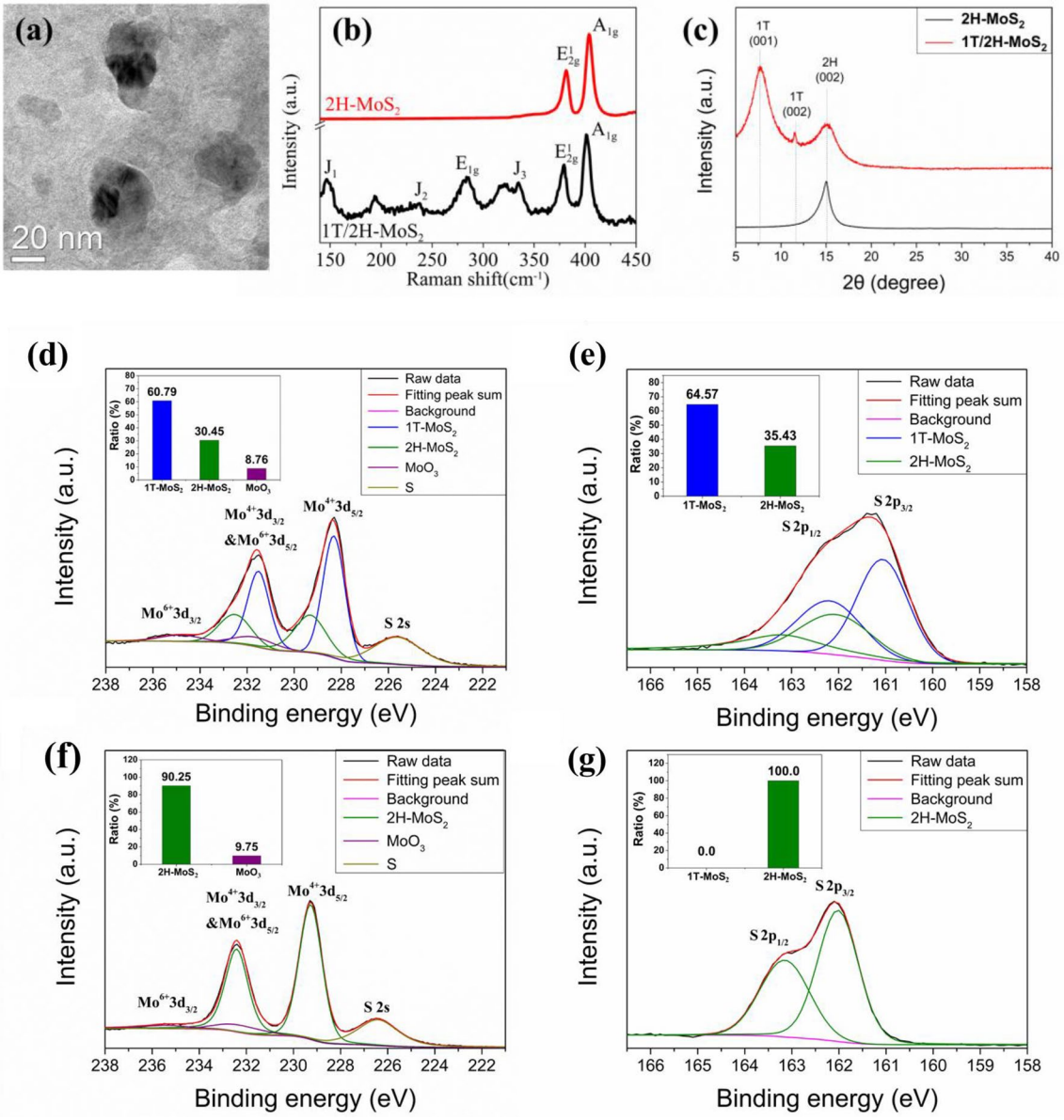

Figure 3. (**a**) TEM micrograph of 1T/2H-MoS_2. (**b**) Raman spectra of 1T/2H-MoS_2 and 2H-MoS_2. and (**c**) XRD patterns of 1T/2H-MoS_2 and 2H-MoS_2. (**d**) XPS spectrum of Mo 3d for 1T/2H-MoS_2. (**e**) XPS spectrum of S 2p for 1T/2H-MoS_2. (**f**) XPS spectrum of Mo 3d for 2H-MoS_2. (**g**) XPS spectrum of S 2p for 2H-MoS_2.

area ratios, the 1T/2H-MoS_2 sample was found to be composed of 64.57% 1T-MoS_2 and 35.43% 2H-MoS_2. In the spectrum for the 2H-MoS_2 sample (Fig. 3g), the 1T-MoS_2 peaks have disappeared due to the heating process. The 2H-MoS_2 S $2p_{1/2}$ and $2p_{3/2}$ peaks were observed at 163.15 eV and 162.02 eV, respectively. The XPS analysis confirms the presence of 1T-MoS_2, 2H-MoS_2, and MoO_3 in the 1T/2H-MoS_2 sample. After heating at 300℃ for 1 h in vacuum, the 1T-MoS_2 was fully transformed into 2H-MoS_2.

The 1T/2H-MoS_2/HDGQDs composite catalyst system was examined by field emission scanning electron microscopy (FE-SEM). As shown in the SEM micrograph in Fig. 4a, the carbon paper substrate composed of carbon fiber filaments are largely covered by the dried solutes of the 1T/2H-MoS_2 and HDGQDs solutions. The distribution of each element shown in Fig. 4b-e indicates that the MoS_2, MnO_3, and GQDs are distributed along with each other on the carbon paper substrate.

As shown in Fig. 5a, the J_1, J_2, J_3, and E_{1g} peaks specific to the 1T phase of MoS_2 are present in the Raman spectrum of 1T/2H-MoS_2/HDGQDs, indicating that the 1T-MoS_2 phase still exists in 1T/2H-MoS_2 after HDGQDs doping. However, the A_{1g} peak shifts from 401.73 to 404.52 cm^{-1} and the E^1_{2g} peak from 380.07 to 377.98 cm^{-1} in the Raman spectrum of 1T/2H-MoS_2 for the 1T/2H-MoS_2/HDGQDs compared to that for the 1T/2H-MoS_2. These peak shifts indicate that the HDGQDs are likely chemically bonded with 1T/2H-MoS_2 to form a composite catalyst[37,38]. Figure 5b shows the XRD patterns of 1T/2H-MoS_2, HDGQDs, and 1T/2H-MoS_2/HDGQDs. The additional peak at $2\theta = 26.0°$ for the 1T/2H-MoS_2/HDGQDs sample, is due to the (002) planes of GQDs. The above XRD results demonstrate that we have successfully synthesized the 1T/2H-MoS_2/HDGQDs composite materials[39]. As shown in Fig. 5c,d, the peak positions of Mo^{6+} $3d_{5/2}$& Mo^{4+} $3d_{3/2}$ and Mo^{4+} $3d_{5/2}$ were lowered by

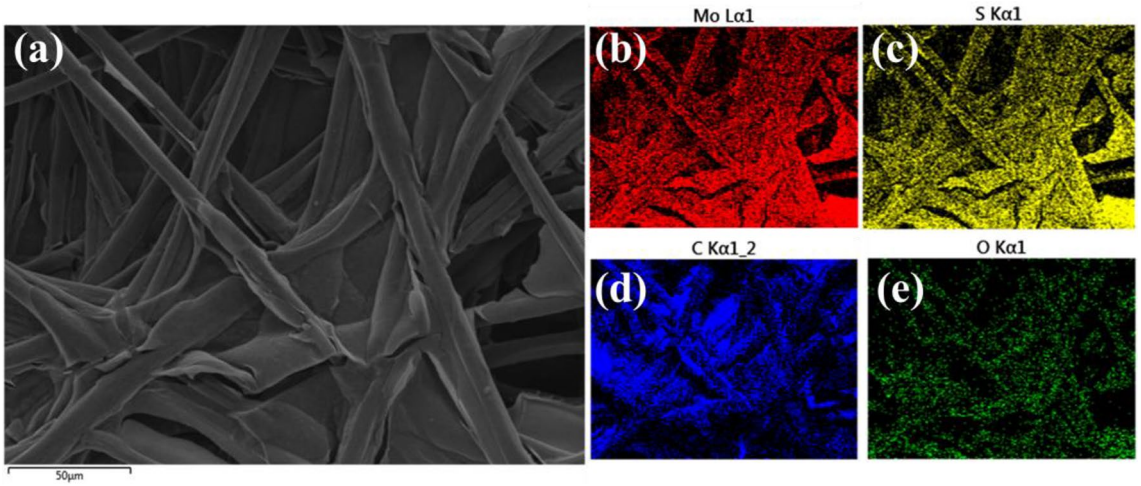

Figure 4. (**a**) SEM image of 1T/2H-MoS_2/HDGQDs on carbon paper substrate. (**b**—**e**) SEM mapping images of different elements of 1T/2H-MoS_2/HDGQDs electrode.

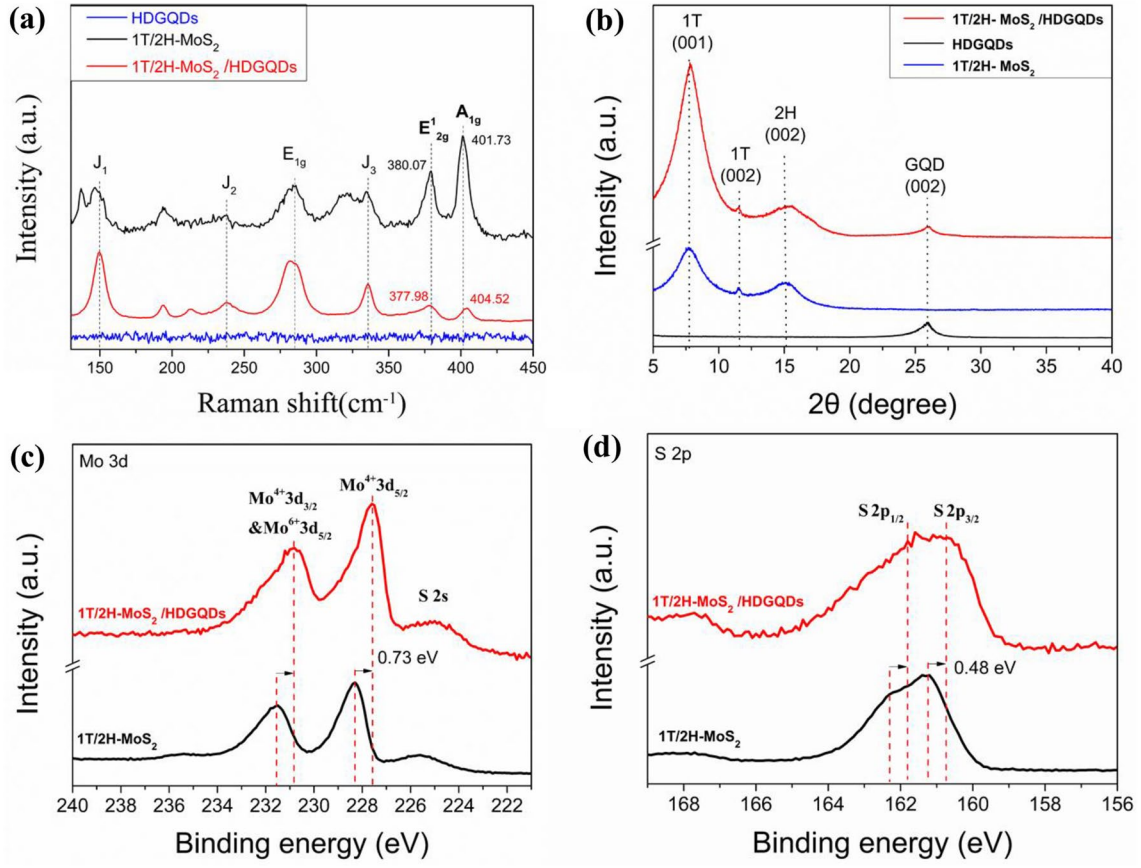

Figure 5. (**a**) The Raman spectra. (**b**) XRD patterns of 1T/2H-MoS_2, 1T/2H-MoS_2/HDGQDs, and HDGQDs. (**c**) XPS spectra of Mo 3d for 1T/2H-MoS_2 and 1T/2H-MoS_2/HDGQDs. (**d**) XPS spectra of S 2p for 1T/2H-MoS_2 and 1T/2H-MoS_2/HDGQDs.

0.73 eV and those of S $2p_{1/2}$ and S $2p_{3/2}$ by 0.48 eV for 1T/2H-MoS_2/HDGQDs compared to those for 1T/2H-MoS_2 in the XPS spectra, indicating charge transfer from HDGQDs to MoS_2[12]. Such charge transfer also evidences the chemical bonding between HDGQDs and 1T/2H-MoS_2. The GQDs-to-MoS_2 charge transfer can improve the efficiency of MoS_2 in adsorbing protons[12].

The LSV curves and Tafel plots for all samples are shown in Fig. 6a,b, respectively. The overpotential and Tafel slope that showcase the electrocatalytic activity for each sample are plotted in Fig. 6c [40]. As shown in Fig. 6c, the

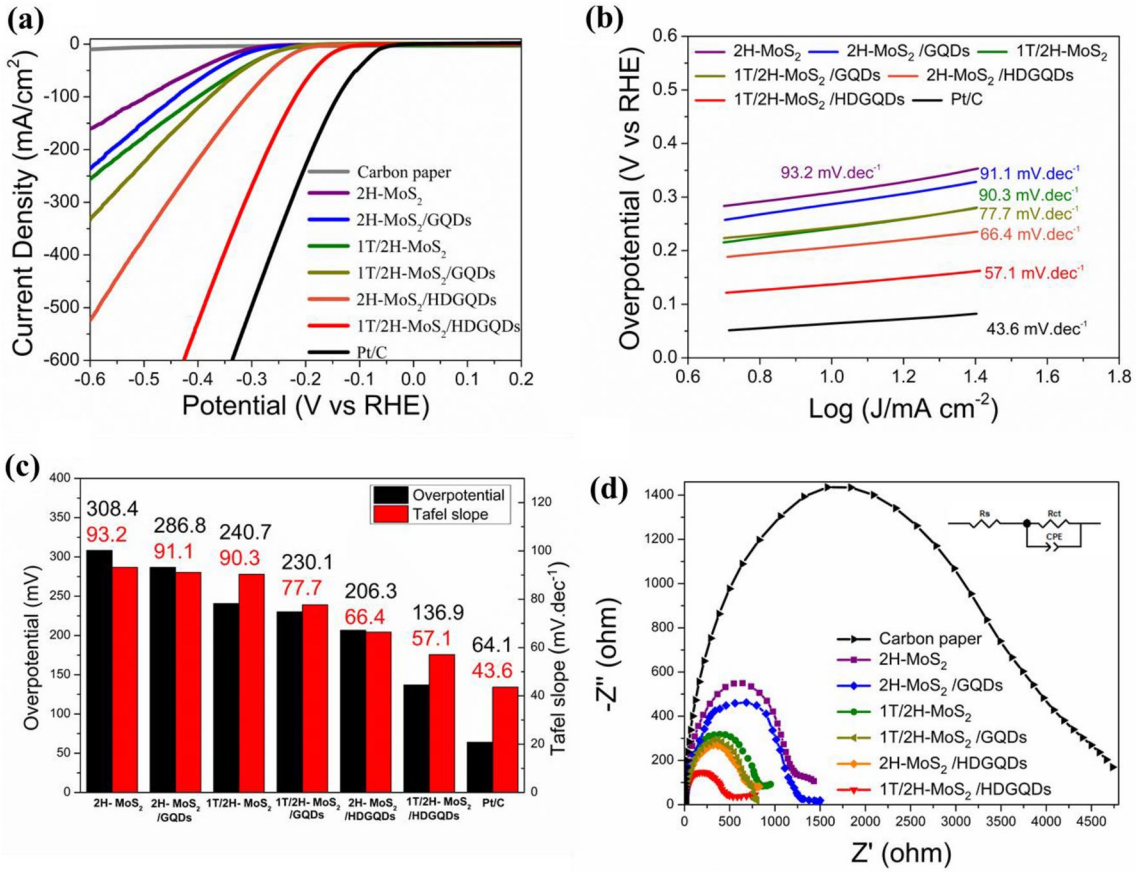

Figure 6. (**a**) Linear sweep voltammetry. (**b**) Tafel plots. (**c**) A duel bar chart to show the overpotentials and Tafel slopes of all samples. (**d**) Electrochemical impedance spectroscopy (EIS).

overpotential and Tafel slope for 1T/2H-MoS_2 are smaller than those for 2H-MoS_2, indicating better electrocatalytic activity for 1T/2H-MoS_2 compared to that for 2H-MoS_2. We can also see that the electrocatalytic activities for both 1T/2H-MoS_2 and 2H-MoS_2 were significantly improved when the standard GQDs were incorporated into the samples, while the catalytic activity of the pure HDGQDs and GQDs electrode can be considered negligible (Supplementary Figure S4). Further activity improvement can be achieved by replacing the standard GQDs with the HDGQDs. The best electrocatalytic activity for the MoS_2/GQDs systems was found in the 1T/2H-MoS_2/HDGQDs sample, of which the overpotential and Tafel slope of 136.9 mV and 57.1 mV/decade were significantly improved towards the Pt/C values of 64.1 mV and 43.6 mV/decade, respectively.

Figure 6d shows the Nyquist diagrams obtained from the electrochemical impedance spectroscopy (EIS) for all samples, as well as the carbon paper substrate. The corresponding equivalent circuit which consists of solution resistance, R_s, charge-transfer resistance, R_{ct}, and constant phase element (CPE) is also shown in the inset of Fig. 6d. The EIS parameters (R_s, R_{ct}, CPE, and the value of the exponent of the CPE (n)) obtained from curve-fitting the Nyquist diagrams using the Zview package[41] are listed in Table 1.[18,42–45] The charge transfer resistance (R_{ct}), that originates from the electronic and ionic resistances at the electrode–electrolyte interface, reflects the kinetics of the catalyzed hydrogen evolution reaction[10].

Sample	R_s, Ω	R_{ct}, Ω	CPE, mF	n
Carbon paper	1.5 ± 8.2	3963.0 ± 137.0	0.91 ± 0.03	0.918 ± 0.014
2H-MoS_2	1.5 ± 1.8	1256.3 ± 32.7	2.99 ± 0.08	0.929 ± 0.011
2H-MoS_2/GQDs	1.5 ± 1.9	1147.1 ± 34.6	1.26 ± 0.09	0.915 ± 0.038
1T/2H-MoS_2	1.5 ± 4.1	866.7 ± 22.2	3.37 ± 0.08	0.870 ± 0.006
1T/2H-MoS_2/GQDs	1.5 ± 0.4	747.1 ± 20.3	4.50 ± 0.20	0.861 ± 0.028
2H-MoS_2/HDGQDs	1.5 ± 0.6	714.9 ± 23.4	5.57 ± 0.18	0.889 ± 0.015
1T/2H-MoS_2/HDGQDs	1.5 ± 1.1	537.4 ± 22.6	5.98 ± 0.38	0.808 ± 0.028

Table 1. The EIS parameters obtained from fitting Nyquist diagrams with the equivalent circuit. Rs is the solution resistance. R_{ct} is the charge-transfer resistance. CPE is the constant phase element, and n is the value of the exponent of CPE.

The R_{ct} values measured for Carbon paper, 2H-MoS_2, 2H-MoS_2/GQDs, 1T/2H-MoS_2, 1T/2H-MoS_2/GQDs, 2H-MoS_2/HDGQDs, and 1T/2H-MoS_2/HDGQDs are 3963.0 ,1256.3 ,1147.1 ,866.7 ,747.1 ,714.9, and 537.4 Ω, respectively. We can see that, as expected, the metallic-1T-MoS_2-rich 1T/2H-MoS_2 sample has a lower R_{ct} compared to that of the semiconducting 2H-MoS_2 sample. When standard GQDs are added to the MoS_2 samples, both the 2H-MoS_2 and 1T/2H-MoS_2 samples show reduced charge-transfer resistance, indicating GQDs have effectively improved the electrode-to-electrolyte charge transfer of the composite catalytic systems. The conductivity can be further improved by replacing the standard GQDs with HDGQDs. We observed the lowest R_{ct} of 537.4 Ω in the 1T/2H-MoS_2/HDGQDs sample, which was dramatically lower than the 2H-MoS_2 value of 1256.3 Ω.

It has been reported that GQDs can generate abundant defect sites on the basal plane and edge plane of MoS_2.[10] These defect sites facilitate electron transfer from GQDs to MoS_2.[10] It has also been reported that enhanced GQDs-to-MoS_2 charge transfer can improve MoS_2's efficiency in adsorbing protons.[12] As demonstrated in our XPS analysis above, we did observe charge transfer from HDGODs to MoS_2 in our sample. In this work, we use highly defective GQDs to increase the number of defect sites introduced by GQDs, so as to enhance the GQDs-to-MoS_2 charge transfer, further promoting MoS_2's efficiency in adsorbing protons and therefore greatly reducing R_{ct} in our catalyzed HER.

According to the above EIS analysis, by selecting 1T/2H-MoS_2 and HDGQDs to construct our composite catalyst system, we were able to greatly reduce the charge transfer resistance in the catalyzed hydrogen evolution reaction. Furthermore, while 2H-MoS_2 only has active sites on the edge plane, 1T-MoS_2 has active sites on the edge plane and basal plane.[3,4,46,47] When doped with the HDGQDs, 1T/2H-MoS_2 is likely to have more defects near the active sites. The improved electrode-to-electrolyte charge transfer, larger number of active sites, and additional defects appear to have synergistically led to the greatly enhanced electrocatalytic activity observed in the 1T/2H-MoS_2/HDGQDs composite catalyst for hydrogen evolution reactions.[3–10,46,47].

Finally, a continuous long-term operation of 1000 cycles and a 24-h chronopotentiometry[29,48–50] were conducted for the 1T/2H-MoS_2/HDGQDs sample to test its stability. As shown in Fig. 7a, no appreciable difference was found between the LSV curve obtained after 1000 cycles and the initial curve. The chronopotentiometry curve in Fig. 7b shows that the overpotential with a constant current density of 10 mA/cm^2 was maintained at a stable level for 24 h. As shown in the inset in Fig. 7b, the LSV curves before and after the 24-h chronopotentiometry measurement showed no appreciable difference either. Therefore, our 1T/2H-MoS_2/HDGQDs composite catalyst appears to be very stable for HER applications.

Conclusion

We have designed and successfully fabricated an efficient composite catalyst system, consisting of a metallic-1T-MoS_2-rich 1T/2H-MoS_2 and a HDGQDs components of particle sizes around 20–40 and 3-5 nm, respectively, for the hydrogen evolution reaction. The 1T/2H-MoS_2 component was prepared by using an improved process involving a heated mixing of MoS_2 powder with n-Butyl lithium in an autoclave reactor and a dialysis procedure to significantly expedite the production of 1T-MoS_2. By using a shortened heating time in pyrolyzing citric acid, we were able to introduce a large number of defects in the GODs product to form HDGQDs, as shown by Raman spectroscopy. While FTIR and XPS data revealed the presence of many functional groups in the HDGQDs that may promote catalytic activity, the XPS data demonstrated that the 1T phase of MoS_2 is dominant in our 1T/2H-MoS_2. The FESEM micrographs of the composite catalysts show that both the HDGQDs and 1T/2H-MoS_2 components distribute along with each other on the carbon paper substrate. The peak shifts in the Raman and XPS spectra of the 1T/2H-MoS_2/HDGQDs compared to those of the undoped 1T/2H-MoS_2 indicate successful GQDs doping. Electrochemical measurements show an overpotential of 136.9 mV and Tafel slope of 57.1 mV/decade for the composite catalyst system in HER, demonstrating a large improvement toward the Pt/C values of 64.1 mV and 43.6 mV/decade, respectively. The improved electrode-to-electrolyte charge transfer indicated by EIS data, larger number of active sites in 1T-MoS_2, and additional defects introduced by

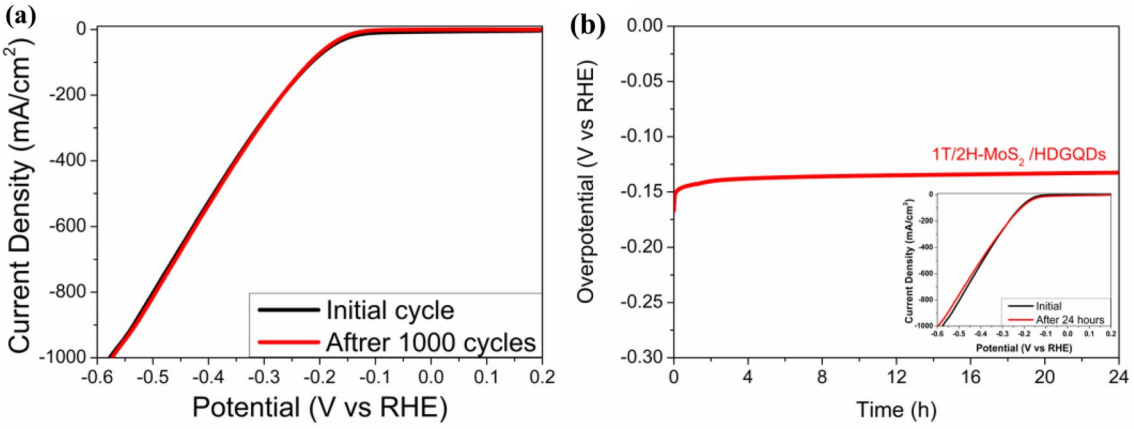

Figure 7. Stability test: (**a**) 1000 LSV cycles and (**b**) The chronopotentiometry curve recorded at a constant cathodic current density of -10 (mA cm^{-2}). Inset shows the linear sweep voltammetry polarization curves before and after the 24-h chronopotentiometry.

HDGQDs doping have synergistically led to the observed electrocatalytic activity enhancement for HER in our composite catalyst system.

Data availability

All data generated or analyzed during this study are included in this published article.

Received: 8 May 2023; Accepted: 10 September 2023
Published online: 13 September 2023

References

1. Yan, Y., Xia, B., Xu, Z. & Wang, X. Recent development of molybdenum sulfides as advanced electrocatalysts for hydrogen evolution reaction. *ACS Catal.* **4**, 1693–1705 (2014).
2. Hinnemann, B. *et al.* Biomimetic hydrogen evolution: MoS_2 nanoparticles as catalyst for hydrogen evolution. *J. Am. Chem. Soc.* **127**, 5308–5309 (2005).
3. Tsai, C., Pedersen, F. A. & Nørskov, J. K. Tuning the MoS_2 edge-site activity for hydrogen evolution via support interactions. *Nano Lett.* **14**, 1381–1387 (2014).
4. Wang, D. *et al.* Polytype 1T/2H MoS_2 heterostructures for efficient photoelectrocatalytic hydrogen evolution. *Chem. Eng. J.* **330**, 102–108 (2017).
5. Li, Y. *et al.* Interface engineering of transitional metal sulfide–MoS_2 heterostructure composites as effective electrocatalysts for water-splitting. *J. Mater. Chem. A.* **9**, 2070–2092 (2021).
6. Li, Y. *et al.* Selective preparation of 1T- and 2H-phase MoS_2 nanosheets with abundant monolayer structure and their applications in energy storage devices. *ACS Appl. Energy Mater.* **3**, 998–1009 (2020).
7. Fan, H. *et al.* Synthesis of metal-phase-assisted 1T@2H-MoS_2 nanosheet-coated black TiO_2 spheres with visible light photocatalytic activities. *J Mater Sci.* **53**, 10302–10312 (2018).
8. Yao, Y., Ao, K., Lv, P. & Wei, Q. MoS_2 coexisting in 1T and 2H phases synthesized by common hydrothermal method for hydrogen evolution reaction. *Nanomaterials* **9**(6), 844 (2019).
9. Wang, S. *et al.* Ultrastable in-plane 1T–2H MoS_2 heterostructures for enhanced hydrogen evolution reaction. *Adv. Energy Mater.* **8**, 1801345 (2018).
10. Guo, J., Zhu, H., Sun, Y., Tang, L. & Zhang, X. Doping MoS_2 with graphene quantum dots: structural and electrical engineering towards enhanced electrochemical hydrogen evolution. *Electrochim. Acta* **211**, 603–610 (2016).
11. Guo, B. *et al.* Coral-shaped MoS_2 decorated with graphene quantum dots performing as a highly active electrocatalyst for hydrogen evolution reaction. *ACS Appl. Mater. Interfaces.* **9**, 3653–3660 (2017).
12. Gong, J. *et al.* Graphene quantum dots assisted exfoliation of atomically-thin 2D materials and as-formed 0D/2D van der Waals heterojunction for HER. *Carbon* **184**, 554–561 (2021).
13. Zhao, S. *et al.* Carbon quantum dots modified MoS_2 with visible-light-induced high hydrogen evolution catalytic ability. *Carbon* **99**, 599–606 (2016).
14. Dong, Y. *et al.* Blue luminescent graphene quantum dots and graphene oxide prepared by tuning the carbonization degree of citric acid. *Carbon* **50**, 4738–4743 (2012).
15. Liu, G. *et al.* MoS_2 monolayer catalyst doped with isolated Co atoms for the hydrodeoxygenation reaction. *Nat. Chem. Vol.* **9**, 810–816 (2017).
16. Eda, G. *et al.* Photoluminescence from chemically exfoliated MoS_2. *Nano Lett.* **11**, 5111–5116 (2011).
17. User Manual Model 600D Series electrochemical analyzer/workstation; CH Instruments, (2012).
18. Pataniya, P. M. & Sumesh, C. K. MoS_2 nanosheets on Cu-foil for rapid electrocatalytic hydrogen evolution reaction. *J. Electroanal. Chem.* **912**, 116270 (2022).
19. Wang, L., Lee, C. Y. & Schmuki, P. Solar water splitting: preserving the beneficial small feature size in porous a-Fe_2O_3 photoelectrodes during annealing. *J. Mater. Chem. A* **1**, 212 (2013).
20. Wu, H. *et al.* Regulating the allocation of N and P in codoped graphene via supramolecular control to remarkably boost hydrogen evolution. *Energy Environ. Sci.* **12**, 2697 (2019).
21. Wu, J., Wang, P., Wang, F. & Fang, Y. Investigation of the microstructures of graphene quantum dots (GQDs) by surface-enhanced raman spectroscopy. *Nanomaterials* **8**, 864 (2018).
22. Yang, Y., Yang, S., Ding, G. & Liu, Z. Self-feedback autocatalysis in free radical triggered photosynthesis of N-doped graphene quantum dots. *Synth. Met.* **271**, 116643 (2021).
23. Du, F. P. *et al.* PEDOT:PSS/graphene quantum dots films with enhanced thermoelectric properties via strong interfacial interaction and phase separation. *Sci. Rep.* **8**, 6441 (2018).
24. Morea, M. P., Lohar, P. H., Patil, A. G., Patil, P. O. & Deshmukh, P. K. Controlled synthesis of blue luminescent graphene quantum dots from carbonized citric acid: Assessment of methodology, stability, and fluorescence in an aqueous environment. *Mater. Chem. Phys.* **220**, 11–22 (2018).
25. Zhu, S. *et al.* One-step synthesis of fluorescent graphene quantum dots as an effective fluorescence probe for vanillin detection. *RSC Adv.* **11**, 9121–9129 (2021).
26. Naik, J. P., Sutradhar, P. & Saha, M. Molecular scale rapid synthesis of graphene quantum dots (GQDs). *J. Nanostruct. Chem.* **7**, 85–89 (2017).
27. Guo, T. *et al.* Layered MoS_2@graphene functionalized with nitrogen-doped graphene quantum dots as an enhanced electrochemical hydrogen evolution catalyst. *Chin. Chem. Lett.* **30**, 1253–1260 (2019).
28. Shen, S. *et al.* Graphited carbon black curled nanoribbons simultaneously boosted stability and electrocatalytic activity of 1T-MoS_2/MoO_3 toward hydrogen evolution. *J. Alloy. Compd.* **949**, 169831 (2023).
29. Bolar, S. *et al.* Conducting scaffold supported defect rich 3D rGO-CNT/MoS_2 nanostructure for efficient HER electrocatalyst at variable pH. *Compos. B* **230**, 109489 (2022).
30. Shi, S., Sun, Z. & Hu, Y. H. Synthesis, stabilization and applications of 2-dimensional 1T metallic MoS_2. *J. Mater. Chem. A.* **6**, 23932–23977 (2018).
31. Fan, X. *et al.* Fast and efficient preparation of exfoliated 2H MoS_2 nanosheets by sonication-assisted lithium intercalation and infrared laser-induced 1T to 2H phase reversion. *Nano Lett.* **15**, 5956–5960 (2015).
32. Xia, Z., Tao, Y., Pan, Z. & Shen, X. Enhanced photocatalytic performance and stability of 1T MoS2 transformed from 2H MoS_2 via Li intercalation. *Res. Phys.* **12**, 2218–2224 (2019).
33. Wu, M. *et al.* Metallic 1T MoS_2 nanosheet arrays vertically grown on activated carbon fiber cloth for enhanced Li-ion storage performance. *J. Mater. Chem. A.* **5**, 14061 (2017).
34. Inta, H. R. *et al.* Ionic liquid-intercalated metallic MoS_2 as a superior electrode for energy storage applications. *Chem. Nano. Mat.* **6**, 1–12 (2020).
35. Kheyrabadi, L. K., Koyappayil, A., Kim, T., Cheon, Y. P. & Lee, M. H. A MoS_2@$Ti_3C_2T_x$ MXene hybrid-based electrochemical aptasensor (MEA) for sensitive and rapid detection of Thyroxine. *Bioelectrochemistry* **137**, 107674 (2021).

36. Lonkar, S. P., Pillai, V. V. & Alhassan, S. M. Three dimensional (3D) nanostructured assembly of MoS_2-WS_2/Graphene as high performance electrocatalysts. *Int. J. Hydrogen Energy* **45**, 10475–10485 (2020).
37. Wang, P. *et al.* Enhanced monolayer MoS_2/InP heterostructure solar cells by graphene quantum dots. *Appl. Phys. Lett.* **108**, 163901 (2016).
38. Min, M., Sakri, S., Saenz, G. A. & Kaul, A. B. Photophysical dynamics in semiconducting graphene quantum dots integrated with 2D MoS_2 for optical enhancement in the near UV. *ACS Appl. Mater. Interfaces.* **13**, 5379–5389 (2021).
39. Moghimian, S. & Sangpour, P. One-step hydrothermal synthesis of GQDs-MoS_2 nanocomposite with enhanced supercapacitive performance. *J. Appl. Electrochem.* **50**, 71–79 (2020).
40. Chauhan, P. *et al.* Engineered interfaces of WSe_2/rhenium doped $SnSe_2$ heterostructures nanosheet arrays for superior hydrogen generation and flexible supercapacitor. *Mater. Today Chem.* **26**, 101079 (2022).
41. Cruz-Manzo, S., Greenwood, P. & Chen, R. An impedance model for EIS analysis of nickel metal hydride batteries. *J. Electrochem. Soc.* **164**(7), A1446 (2017).
42. Kuchkaev, A. M. *et al.* Covalent functionalization of black phosphorus nanosheets with dichlorocarbenes for enhanced electrocatalytic hydrogen evolution reaction. *Nanomaterials* **13**, 826 (2023).
43. Shi, H. *et al.* Surface conductance analysis of X-MoS2 (X = Fe Co, Ni) prepared on graphite felt as bifunctional catalysts for the hydrogen/oxidation evolution reactions. *Electrochim. Acta* **439**, 141596 (2023).
44. Pataniya, P. M., Yang, X., Li, B., Kannichankandy, D. & Sumesh, C. K. Enhanced electrocatalysis of WSe_2 nanosheets by partial oxidation for hydrogen generation. *Int. J. Energy Res.* **46**, 12073–12081 (2022).
45. Choi, W., Shin, H. C., Kim, J. M., Choi, J. Y. & Yoon, W. S. Modeling and applications of electrochemical impedance spectroscopy (EIS) for lithium-ion batteries. *J. Electrochem. Sci. Technol.* **11**(1), 1–13 (2020).
46. Manikandan, A. *et al.* A superior dye adsorbent towards the hydrogen evolution reaction combining active sites and phase-engineering of (1T/2H) MoS_2/a-MoO_3 hybrid heterostructured nanoflowers. *J. Mater. Chem. A* **6**, 15320–15329 (2018).
47. Wang, S. *et al.* Ultrastable in-plane 1T–2H MoS_2 heterostructures for enhanced hydrogen evolution reaction. *Adv. Energy Mater* **8**, 1801345 (2018).
48. Sumesh, C. K. Zinc oxide functionalized molybdenum disulfide heterostructures as efficient electrocatalysts for hydrogen evolution reaction. *Int. J. Hydrog.Energy* **45**, 619–628 (2020).
49. Kannichankandy, D., Pataniya, P. M., Sumesh, C. K., Solanki, G. K. & Pathak, V. M. WSe_2-PANI nanohybrid structure as efficient electrocatalyst for photo-enhanced hydrogen evolution reaction. *J. Alloy. Compd.* **876**, 160179 (2021).
50. Feng, B., Liu, C., Yan, W., Geng, J. & Wang, G. MoS_2 nanotubes loaded with TiO_2 nanoparticles for enhanced electrocatalytic hydrogen evolution. *RSC Adv.* **9**, 26487–26494 (2019).

Author contributions

S.F.C., T.S.W., and Y.L.S. conceived and designed the experiments. S.F.C. prepared the materials. S.F.C., T.S.W., and Y.L.S. planned and performed the physical properties characterization and electrochemical measurements. S.F.C., T.S.W., and Y.L.S. co-wrote the paper.

Competing interests

The authors declare no competing interests.

Additional information

Supplementary Information The online version contains supplementary material available at https://doi.org/10.1038/s41598-023-42410-9.

Correspondence and requests for materials should be addressed to T.-S.W. or Y.-L.S.

Reprints and permissions information is available at www.nature.com/reprints.

Publisher's note Springer Nature remains neutral with regard to jurisdictional claims in published maps and institutional affiliations.

Open Access This article is licensed under a Creative Commons Attribution 4.0 International License, which permits use, sharing, adaptation, distribution and reproduction in any medium or format, as long as you give appropriate credit to the original author(s) and the source, provide a link to the Creative Commons licence, and indicate if changes were made. The images or other third party material in this article are included in the article's Creative Commons licence, unless indicated otherwise in a credit line to the material. If material is not included in the article's Creative Commons licence and your intended use is not permitted by statutory regulation or exceeds the permitted use, you will need to obtain permission directly from the copyright holder. To view a copy of this licence, visit http://creativecommons.org/licenses/by/4.0/.

© The Author(s) 2023